Project Number: 766719
Start Date of Project: 2017/11/01

Deliverable 5.2 – V1.0

Report on magneto-transport and electroluminescence measurements

Partners involved: ETH, UNIROMA3, NXT, UGLA

Dissemination level	Confidential
Submission Date	2020/10/31
Work Package	WP5
Task	T5.2; T 5.3
Type	Report
Version	1.0
Author	Giacomo Scalari
Reviewed by	Douglas Paul
Approved by (CO)	Monica De Seta

Disclaimer
The content of this deliverable does not reflect the official opinion of the European Union. Responsibility for the information and views expressed herein lies entirely with the author(s).

Table of Contents

1. Introduction

In the following report measurements of different Ge/SiGe quantum cascade layers with the same target active region design are discussed. Each layer consists of 51 periods of the Delta States Design with $Si_{0.15}Ge_{0.85}$ barriers, see D 5.1. Section 3. The properties of the layers are listed in Table 1. The layers were fabricated to the following device types:

1. Circular transmission line test structures (CTLMS) to determine the bottom and top contact resistances.
2. Circular mesa structures (CMS) with diameter ranging from 50 to 200 um to check the current scaling with device area and to perform magneto-transport measurements.
3. Interdigitated diffraction gratings (IDG) to measure the electroluminescence signal.

Generation	Layer ID	N_{2D} [cm-2]	L_p [nm]	Metallization	Growth direction
II	2289	1.8e11	82.4	AgSb	Direct
	2292	3.6e11	81.0		
III	2306	5e10	85.5	NiGe	
	2307	7e10	83.3		
IV	2315	7e10	87.8		Reversed
	2322	4x 1.75e10	81.5		Direct

Table 1. Layer IDs with the nominal sheet doping density N_{2D} and period length L_p measured by XRD.

2. Transport-Contacts and doping

For the generation II layers, UGLA realized Ohmic contacts to the active region with Ag/Sb(1%) metallization. A specific contact resistivity of 2.5 x 10^{-5} Ωcm^2 was achieved at 10 K. However, this choice of metallization led to adhesion problems of the metals and some devices couldn't be wire-bonded because the whole metallization ripped off. We also believe that for some devices part of the Ag layer oxidised and prevented any current to flow. Facing these problems, we decided to employ a NiGe metallization to form Ohmic contacts for generation III-IV layers envisaging a more stable fabrication process [1]. The lowest specific contact resistivity measured at 10K was 7.8 x 10^{-4} Ωcm^2 (see Figure 1). Note that only a two-point measurement could be employed and the actual contact resistivity is lower.

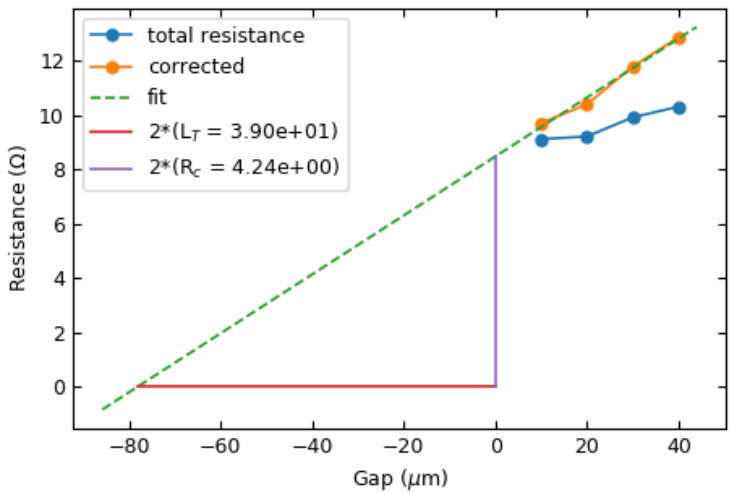

Figure 1: Total resistance for the CTLMS (bottom contacts of layer 2307) as a function of the gap spacing between circular conducting inner and outer region. The total resistance (blue curve) is multiplied by a geometrical correction factor (orange curve). The specific contact resistance, the transfer length L_T and the contact resistance R_c are fitted to the model described in [2].

Even though the contact resistivity increased, the overall device yield for generation III-IV increased due to the cleaner fabrication process with NiGe metallization. Additional improvements in the growth quality by **,** UNIROMA3 resulted in more reproducible current-voltage (VI) characteristics. Devices with the same geometry showed the same VI curves, which is a significant improvement with respect to devices of generation II. This can be seen in Figure 2, where the current density at 1V is depicted as a function of the nominal sheet doping density. Each point corresponds to an average of three devices (except for 2315 and 2322 only two) with the same geometry and the error bar represents the standard deviation.

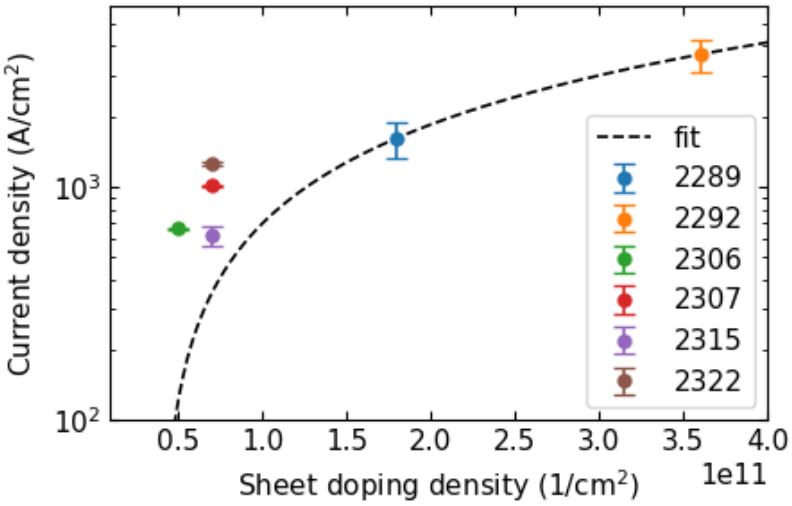

Figure 2. Current density extracted at a bias point of 1V for nominal sheet doping density. Each point and error bar represents the average and standard deviation of three identical device geometries. The linear fit was used to extrapolate the doping for the generation III layers. Note that for layers 2315 and 2322 only two devices of the same geometry were measured.

For samples in generation III and IV the doping and consequently the current density is reduced. The lower current density favours detecting the intersubband emission due to less Joule heating of the device. The device and material quality increased, however a scaling of the current with the device area could not yet be achieved. In Figure 3 the transport behaviour of devices of layer 2307 is depicted. The current density of CMS with varying diameters from 60-100 μm and IDG of two sizes are compared. It can be seen that the current density does not overlay, if the device geometry differs. The current densities also do not scale with the perimeter (not shown here). The measurements are repeatable for devices with the same dimensions. The layers 2306, 2315 and 2322 show a similar behavior. This behavior suggests that the devices are not homogeneously pumped, or that a part of the current is transported along the lateral surface or by defects. Note however that D4.2 suggests that the TD leakage current density is negligible when the TD density is in the low 10^6 cm^{-2} range as in samples 2306, 2315 and 2322.

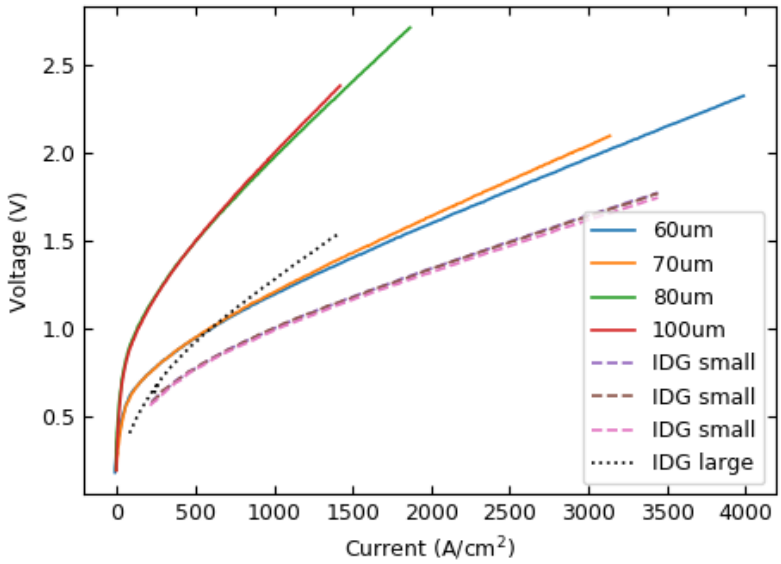

Figure 3. Transport characteristics of layer 2307: Current density of CMS with varying diameter (solid lines), IDG small with an area of 1.1 x 10^{-4} cm^2 (dashed lines), IDG large with an area of 3.3 x 10^{-4} cm^2 (dotted line).

3. Transport and Magneto-transport

The grating devices prepared for electroluminescence were also used to perform magneto-transport measurements. Current-Voltage curves were recorded as a function of the magnetic field in the range 0-10 T at a temperature of 4.2 K (sample immersed in liquid He). As visible from Fig.4(b) the sample exhibits the typical turn-on behaviour as a result of the alignment of the cascade structure and a positive magnetoresistance, as expected from the carrier localization in the plane of the heterostructure. We run calibration measurements on the parent III-V GaAs-based laser structure (N471 Ref.[3]) that are reported in Fig. 4(a,c): we record the current as a function of applied bias and sweep the magnetic field. We successively differentiate the curves with respect to the magnetic field. In this case clear oscillations are observed due to coupling of different Landau levels coming from upper and lower states. Unfortunately, for the Ge/SiGe heterostructure such differential analysis does not reveal reliable features. We do not observe as well any clear sign of band misalignment (NDR) that marks the end of resonant tunneling injection in the upper lasing state in quantum cascade devices. It is expected that in non-polar materials like Ge/SiGe the electronic temperature can be much higher than the lattice one and the resonant tunneling can be affected by this. We believe that the absence of clear signatures of NDR and magneto-related resonances has two main origins:

1. a non-selective injection of the electrons in the upper lasing state (see following paragraph)
2. a low carrier mobility (THz magneto optical measurements performed on the same layers did not show electronic cyclotron transitions up to a field of 8 T.)

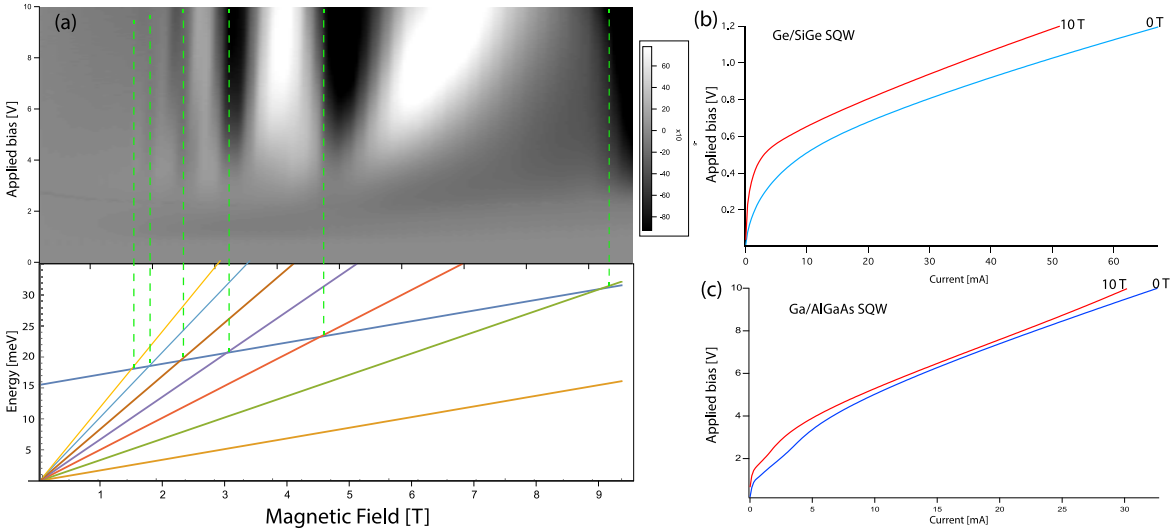

Figure 4. (a): Magnetotransport for GaAs/AlGaAs SQW laser and corresponding Landau Fan. The color scale is refererred to dI/dB. (b): IV curves at 0 and 10 T for Ge/SiGe SQW. (c:) IV curves at 0 and 10 T for GaAs/AlGaAs SQW.

4. Electroluminescence measurements

The energy band diagram for the single quantum well (SQW) Delta States Design is shown in Figure 5. The choice of this design has been discussed in the previous second year report .
The thicknesses are scaled according to the period length of layer 2307 measured by XRD.
The light-current-voltage (LIV) characteristics of the considered layers are shown in Figure 7. The operation points are acquired with relatively low electrical injection power to prevent any blackbody emission overcoming the intersubband signal.
Typical spectra measured on the same IDG geometry of layers 2306, 2307 and 2315 are shown in Figure 6. The biasing voltage for all the electroluminescence measurements is chosen in the range 0.9-1.2 V (see Fig.7).
Due to the low current density inherent to the SQW design the total injected power in the devices at the operation points is at most 210 mW. Two distinguishable peaks appear for the three layers. The peaks are fitted with a double Lorentzian function and compared to the peak position computed with nextano. NEGF for given period length and bias point. The measurements agree to within 2 meV of the simulated peak positions. The observed FWHMs lie in the range 2-3.5 meV ($\Delta f/f \cong 0.2$) and agree well with optical absorption measurements in unbiased quantum wells [4,5]. We attribute the first peak to the vertical transition between the first excited state and ground state in the main quantum well (see red indicated states in Figure 5). The second peak we attribute to transitions between a higher lying energy state and the upper state of the miniband (see blue indicated states in Figure 5). Compared to GaAs quantum cascade structures the second peak is believed to appear due to a weaker electron-phonon interaction which leads to a higher electronic temperature and ultimately to a non- selective electronic injection in the upper state. Such a peak was indeed observed also on GaAs structures above the NDR[6]. The strongest emission is observed from layer 2315 that was grown in the reversed direction with respect to 2306 and 2307.

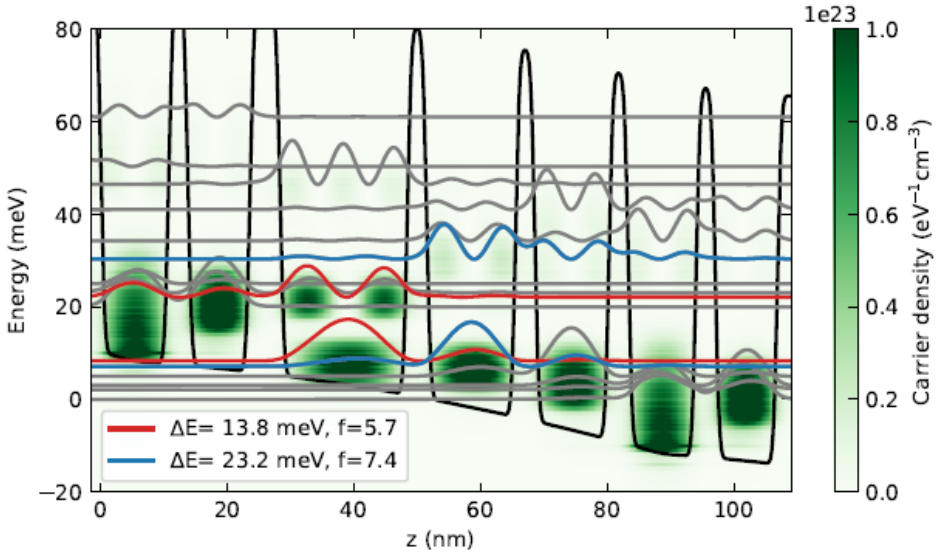

Figure 5. NEGF simulations done with the nextnano.NEGF package at 20mV/period and 10K for the layer 2307. The blackline is the L-valley conduction band-offset and in green is shown the energy resolved carrier density.

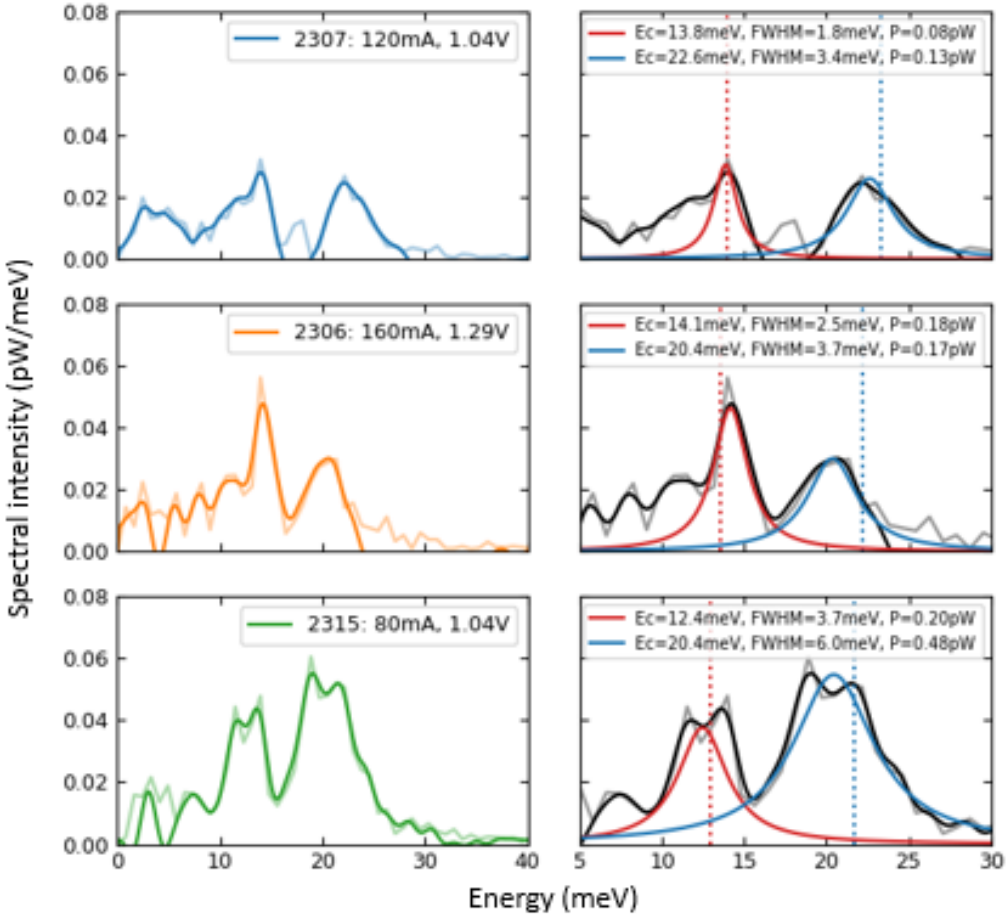

Figure 6. Electroluminescence spectra for layer 2306, 2307 and 2315 (left column). The Lorentzian fits (right column) are compared to the simulated peak positions (vertical dotted lines). The spectra are obtained by taking the Fourier transform of the X component of the lock-in signal.

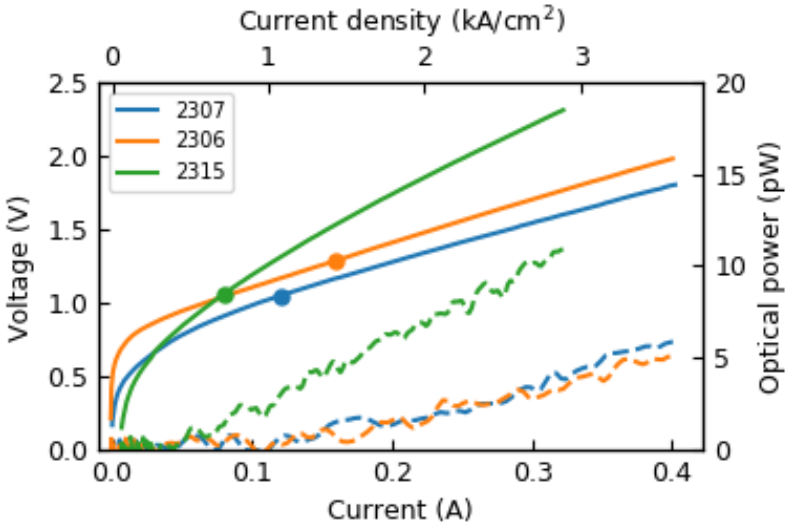

Figure 7. Light current voltage characteristics of layers 2306, 2307 and 2307. The dashed lines are the light-current curves, the solid lines the VI curves and the dots represent the operation point where the spectra of Figure 6 are acquired.

The electroluminescence experiments are performed as described in D 5.1. section 1. To increase the signal to noise ratio, multiple interferograms with the same experimental conditions were averaged yielding typically 8-24 hours of total integration time. With a 2 s integration time per step, the X- and Y-component of the lock-in signal and also the temperature are acquired for every step of the mirror. The measurement overview for the spectra of layer 2307 is shown in Figure 8. The temperature is also stable within 200 mK for most of the measurement time.

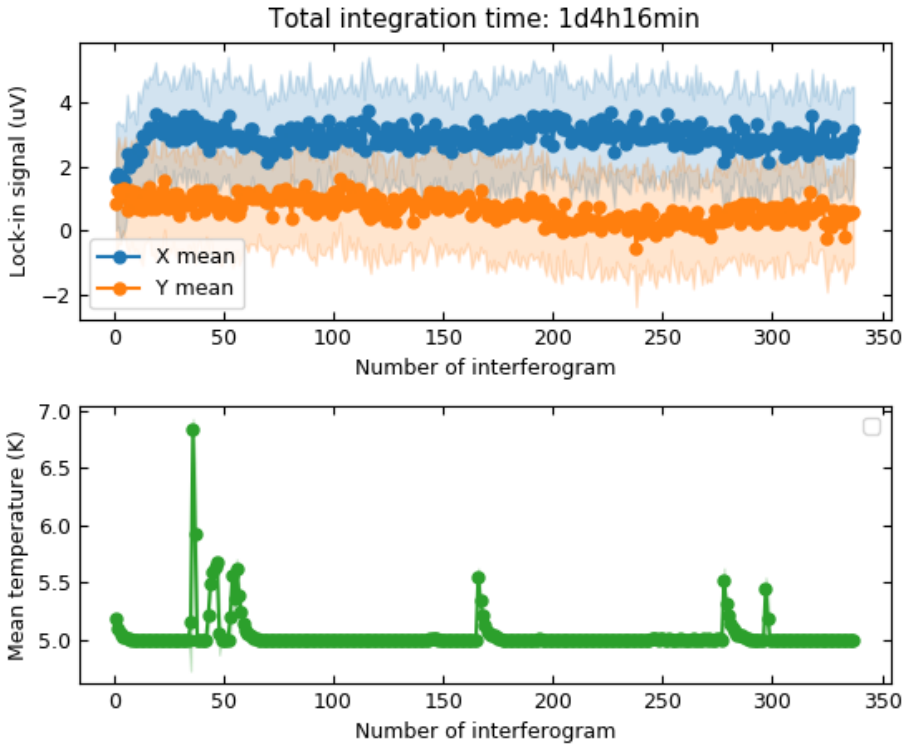

Figure 8: Measurement monitoring for the spectrum of layer 2307 (shown in Figure 5). Top: The mean (dots) and standard deviation (semi-transparent area) of the X- and Y-component of the lock-in signal for each interferogram. Bottom: Mean temperature for every interferogram. Note that the standard deviation is not visible on this scale.

We performed also electroluminescence measurements on a SQW sample (2322) where the doping has been placed in all the quantum wells. This is known to have a detrimental effect on the efficiency and on the broadening of ISB emission. Since this sample has been fabricated with exactly the same gratings as the ones of Fig.6, it constitutes an excellent control sample. The emission from this sample, (operated with the same electrical injected power as the measurements of Fig.6) is reported Fig. 9. The collected signal is much lower than in the other samples, the X component (the one with the correct phase for emission) shows a broad incoherent signal and the Y component is large. So this is a conclusive proof of the ISB nature the electroluminescence signals reported in Fig.6.

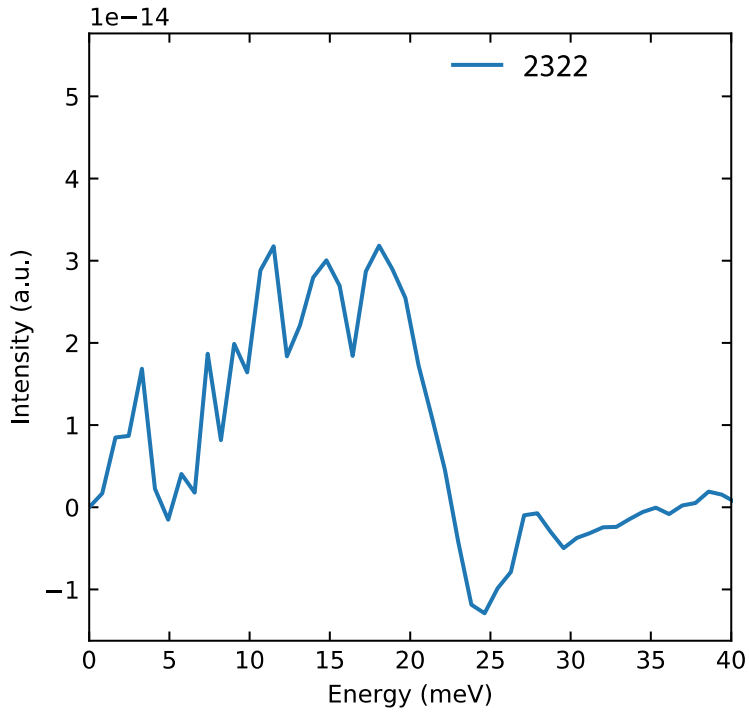

Figure 9: Fourier transform for the X component of sample 2322 (doped in all 4 wells) processed with identical gratings as samples 2306, 2307, 2315.

5. Conclusions

As a conclusion, we observed electroluminescence signals from 3 different epitaxial layers: the strongest emission corresponds to sample 2315, the layer grown in reverse order with respect to the other two. The narrowest peak attributed to the vertical transition in the broad well is observed for sample 2306 (Δf =2.5 meV, f=14.1 meV). The absence of features in the transport makes an estimation of the upper state lifetime difficult and points towards a non-selective injection of electrons in the cascade structure. This is confirmed by the observation of a second, high energy peak in the electroluminescence.

6. Outlook

On the basis of the results above, the following steps are planed:

1) Grating simulations to enhance the detection efficiency.
2) Fabrication of the employed and newly developed grating geometries on similar III-V active region designs, to extract the collection efficiency and to estimate the non-radiative lifetime of the Ge/SiGe material systems.
3) Measurements of a newly designed 4-quantum well structure with a larger confinement energy (i.e. reduced Ge-content in the barriers) and larger gain. The design also accounts for delta states in the barriers.

References:

1. Gallacher, K., et al.*,Ohmic contacts to n-type germanium with low specific contact resistivity.* Applied Physics Letters, 2012, **100**, 022113
2. Dieter K. Schroder *Semiconductor Material and Device Characterization*. John Wiley & Sohns, 2006.
3. Scalari G et al., *Population inversion by resonant tunneling in quantum wells*, Appl. Phys. Lett. 2007, 91 (3), 032103
4. Virgilio M, Sabbagh D, Ortolani M, Di Gaspare L, Capellini G, De Seta M (2014). "Physical mechanisms of intersubband-absorption linewidth broadening in s-Ge/SiGe quantum wells" Phys. Rev. B 90, 155420 (2014)
5. Ciano C et al., *Control of Electron-State Coupling in Asymmetric Ge/Si-Ge Quantum Wells.* Physical Review Applied, 2019, **11**, 014003
6. Rochat M et al., *Far-infrared (lambda 88 μm) electroluminescence in a quantum cascade structure*, Appl. Phys. Lett. 1998, 73,25